Supporting information to 'Electrostatically confined monolayer graphene quantum dots with orbital and valley splittings'

Nils Michael Freitag,[†] Larisa A. Chizhova,[‡] Peter Nemes-Incze,[†] Colin R. Woods,[¶] Roman Vladislavovich Gorbachev ,[¶] Yang Cao,[¶] Andre K. Geim,[¶] Kostya S. Novoselov,[¶] Joachim Burgdörfer,[‡] Florian Libisch,[‡] and Markus Morgenstern[*,†]

[†]II. Institute of Physics B and JARA-FIT, RWTH Aachen University, Otto-Blumenthal-Straße, 52074 Aachen, Germany

[‡]Institute for Theoretical Physics, TU Wien, Wiedner Hauptstraße 8-10, 1040 Vienna, Austria, EU

[¶]School of Physics & Astronomy, University of Manchester, Manchester, United Kingdom

E-mail: MMorgens@physik.rwth-aachen.de

Fax: 0049 241 80 22306

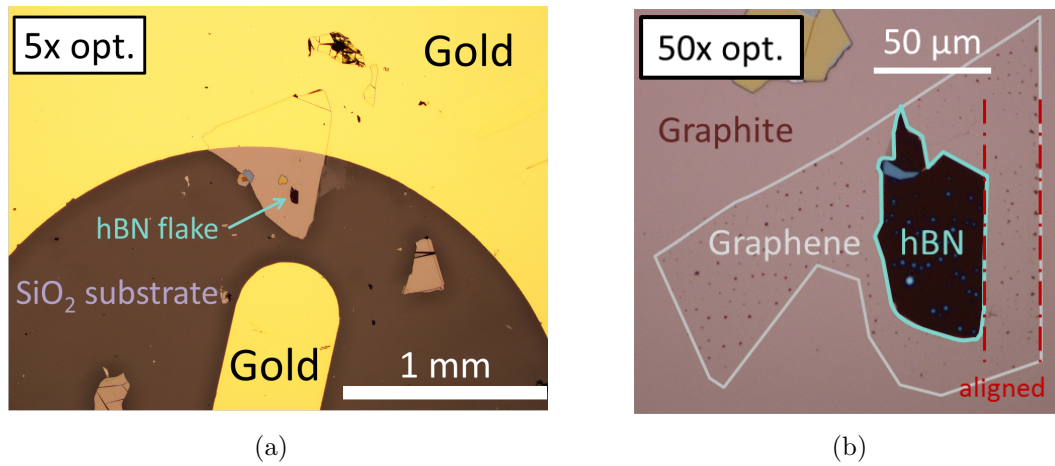# Contents

1 Sample preparation

Figure S1: **(a)** 5× enlarged optical image of the sample. **(b)** 50× enlarged optical image zooming onto the graphite/BN/graphene stack.

The device structure shown in Figure 1a of the main text was prepared by exfoliating graphite flakes on a SiO_2 substrate, followed by two consecutive dry transfers[1,2] of $30\,nm$ thick hexagonal BN and monolayer graphene. As shown in Figure S1b, the graphene flake overlaps the BN completely to avoid insulating areas, which are potentially hazardous to the STM tip. Figure S1a shows the graphene flake with electrical Au contacts prepared via shadow mask evaporation of Cr/Au $(2\,nm/100\,nm)$ onto the large bottom graphite flake. This design does not allow for back-gate operation. During the transfer of graphene onto BN, great care was taken to keep the misalignment of both crystal lattices to about $0°$.[3]

2 STM measurement details

Tungsten tips were prepared by microchemical etching of wires. The microtips were then reshaped by controlled indentation into the surface of a Au(111) crystal,[4] thereby forming a Au apex of a few 10 nm in length. We characterize the tips by exploiting the topographic and spectroscopic features of the Au(111) surface reconstruction. The tip's work function is reduced compared to bulk Au and is expected to lie in the range of $4.5 - 4.8\,\mathrm{eV}$.[5,6]

Scanning tunneling microscopy (STM) images were measured in constant current mode, where the feedback loop adjusts the tip-sample distance $d_{\mathrm{tip-gr}}$ to keep the tunneling current I constant. Scanning the sample and tracking the tip's z-position reveals the so-called topography.

The differential conductance dI/dV curves were measured by lock-in detection of the tunneling current change due to modulation of the tip voltage V_{tip} with a frequency of $f_{\mathrm{mod}} = 1223\,\mathrm{Hz}$ and amplitudes of $V_{\mathrm{mod}} = 2 - 5\,\mathrm{mV_{rms}}$. We optimized V_{mod} for well separated charging peaks at maximum signal-to-noise ratio. Prior to sweeping V_{tip} for every spectrum, the tip is stabilized at the stabilization voltage V_{stab} and current I_{stab}. Then the feedback loop is switched off for the acquisition of the $I(V_{\mathrm{tip}})$ and $dI/dV(V_{\mathrm{tip}})$ spectrum. Whenever we plot $(dI/dV)/I_0$, we divide every point of the dI/dV spectrum by the first current value $I_0 = I(V_{\mathrm{stab}})$ of the measured $I(V)$ curve. This normalization compensates small remaining variations in tip-sample distance after stabilization, which are due to inherently imperfect feedback loop operation or residual mechanical noise.

Compared to usual dI/dV measurements, where the tip-sample distance is kept constant after stabilization, the presented data was collected in the varied-Z mode, where the tip slightly approaches the sample at a rate of $50\,\mathrm{pm/V}$. Thus the tip approached the sample by $0.5\,\text{Å}$ while sweeping the voltage from $1\,\mathrm{V}$ to $0\,\mathrm{V}$ and retracted the same distance while continuing to sweep to $-1\,\mathrm{V}$. This increases the visibility of features for small V_{tip} in the spectrum. In turn, graphene's linear density of states (at $0\,\mathrm{T}$) will not appear in its usual 'V-shape' in dI/dV, but comparatively flat. The additionally ensued change in tip to sample
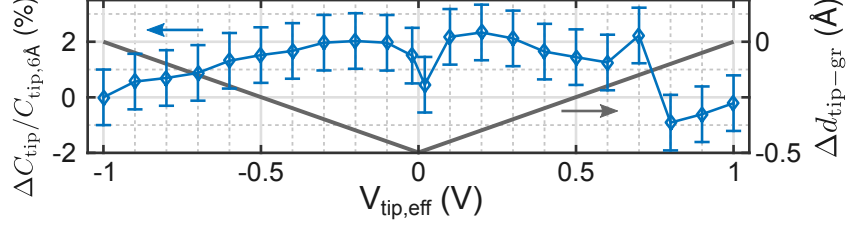
Figure S2: Relative change of the tip to dot capacitance $\Delta C_{\mathrm{tip}} = C_{\mathrm{tip,VarZ}} - C_{\mathrm{tip,6\mathring{A}}}$ with respect to the situation with fixed tip-sample separation $d_{\mathrm{tip-gr}} = 6\,\mathring{A}$. During the varied-Z spectroscopy, the tip approaches by $\Delta d_{\mathrm{tip-gr}} = 0.5\,\mathring{A}/\mathrm{V}$. Poisson calculation for $r_{\mathrm{tip}} = 120\,\mathrm{nm}$ and $r_{\mathrm{dot}} = 25\,\mathrm{nm}$. $V_{\mathrm{tip,eff}}$ denotes the applied tip voltage. The error bars reflect the convergence criterion of the Poisson solver concerning the iteration-by-iteration threshold in the change of the induced charge, which is used to calculate the capacitance. More details in section 'Poisson solver'.

capacitance, derived from our Poisson-solver results and shown in Figure S2, amounts to below $2.5\,\%$. It was thus neglected, since the capacitance uncertainty due to the uncertainty in tip radius is larger (Fig. S4).
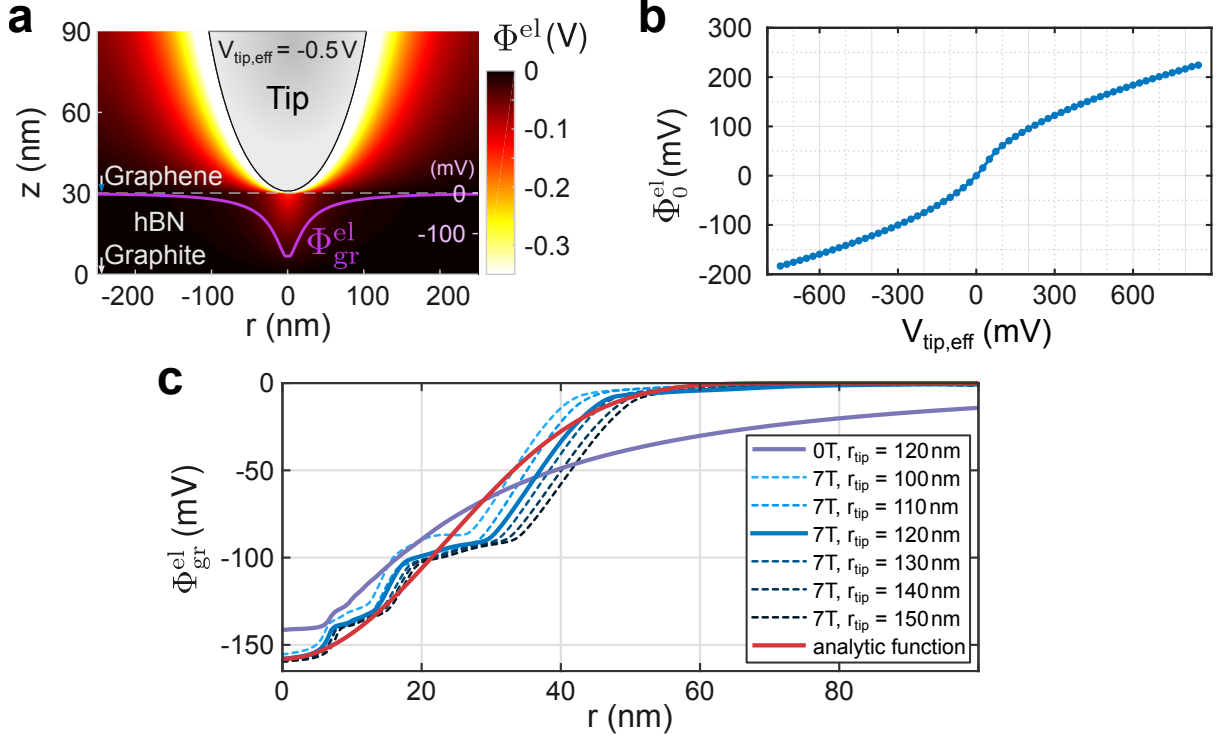
3   Poisson solver

Figure S3: **(a)** Converged numerical solution of Poisson's equation modeling the STM tip ($r_{\text{tip}} = 120\,\text{nm}$, $d_{\text{tip}-\text{gr}} = 6\,\text{Å}$) over graphene ($\varepsilon_{\text{gr}} = 2.5$, Fermi velocity $\nu_{\text{F}} = 1 \times 10^6\,\text{m/s}$) on BN ($\varepsilon_{\text{BN}} = 4$, $t_{\text{BN}} = 30\,\text{nm}$) on graphite (potential fixed to ground) at $B = 0\,\text{T}$. Induced hole confinement potential in the graphene layer $\Phi_{\text{gr}}^{\text{el}}$ as magenta overlay. **(b)** Tip-induced potential amplitude Φ_0^{el} depending on the effective applied tip voltage $V_{\text{tip,eff}}$, which includes possible work function differences between graphene and tip at $B = 0\,\text{T}$. Every dot corresponds to a separate calculation. **(c)** Change in $\Phi_{\text{gr}}^{\text{el}}(r)$ for varying r_{tip} and applied magnetic fields. Red curve portrays the potential used in the TB calculation, corresponding to eq 1.

In order to model the electrostatic tip-sample interaction, we first solve Poisson's equations numerically, using an iterative finite-difference method, for the complete problem (i.e., tip, graphene, BN, graphite) to evaluate the tip-induced potential. We used a tip radius $r_{\text{tip}} = 120\,\text{nm}$, a tip sample distance $d_{\text{tip}-\text{gr}} = 6\,\text{Å}$, the thickness of the BN layer $t_{\text{BN}} = 30\,\text{nm}$, the dielectric constants of BN $\varepsilon_{\text{BN}} = 4$ and graphene $\varepsilon_{\text{gr}} = (4+1)/2 = 2.5$, a magnetic field $B = 0\,\text{T}$ or $7\,\text{T}$ to model the density of states of graphene including $3\,\text{meV}$ disorder broadening and a temperature of $T = 8\,\text{K}$. The grounded graphite is modeled by the boundary condition $\Phi^{\text{el}}(z = 0\,\text{nm}) = 0\,\text{V}$. Figure S3a shows an exemplary converged solution of the

resulting potential (color code) with the potential within the graphene layer $\Phi_{\text{gr}}^{\text{el}}$ as magenta overlay.

We perform calculations with varying tip potential to find the relation $\Phi_0^{\text{el}}(V_{\text{tip,eff}})$ in Figure S3b, which we use to translate tip-induced potential amplitudes Φ_0^{el} to tip voltages and vice versa. Here, we use the effective tip voltage $V_{\text{tip,eff}} = V_{\text{tip}} + \Delta\Phi/e$, to simplify the discussion by making the applied tip voltage V_{tip} independent of any work function difference $\Delta\Phi = \Phi_{\text{tip}} - \Phi_{\text{graphene}}$, which only presents an offset.

We also estimate the effect of an external magnetic field B on the band bending. Therefore we implement LLs into graphene's DOS at energies following eq 1 of the main text, degeneracy $n_{\text{LL}} = 4 \times \frac{e}{hB}$, and smoothed by a Gaussian with standard deviation $\sigma = 3\,\text{meV}$. The main effect of the increased DOS close to E_{F} is a reduction of the radial tail of the induced potential, as seen in Figure S3c.

We use the results at $B = 7\,\text{T}$ to deduce an analytic function for the induced potential (red curve in Fig. S3c) reading

$$\Phi_{\text{gr}}^{\text{el}}(\Phi_0^{\text{el}}, r) = \Phi_0^{\text{el}} \cdot \cos\left(\frac{\pi r}{2\Phi_0^{\text{el}}} \cdot \frac{10^6}{0.32 + \left(\frac{0.005 + |\Phi_0^{\text{el}}|}{0.04} \right)^{-1.2}} \right)^5, \tag{1}$$

where Φ_0^{el} in [V] is the induced electric potential amplitude and r in [m] is the radial distance to the center of the tip. This simplifies the implementation into the tight binding (TB) calculations, because Φ_0^{el} is the only free parameter. The cos-shape was motivated by work of Maksym et al.[7], while the regularly suggested Gaussian[8] would only suit tips with very small radii $r_{\text{tip}} \leq 20\,\text{nm}$. We used $r_{\text{tip}} = 120\,\text{nm}$, though results only vary slightly for $100\,\text{nm} \leq r_{\text{tip}} \leq 150\,\text{nm}$ as shown in Figure S3c. However, if we go to $r_{\text{tip}} < 70\,\text{nm}$, the TB results strongly differ from the experimental observations. The tip radius is thus our main parameter to match theory and experiment.

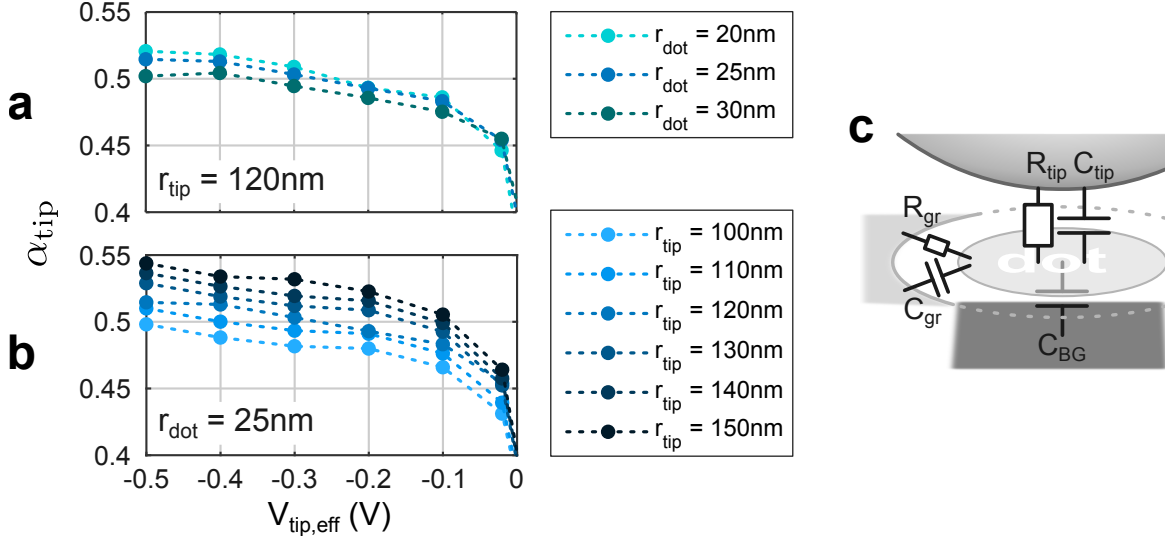# 4   Capacitances, tip lever arm and tunnel-coupling of QD states

Figure S4: **(a)** Change in tip lever arm α_{tip} due to a changing dot radius r_{dot} at constant tip radius $r_{\text{tip}} = 120\,\text{nm}$. **(b)** Change in α_{tip} for varying r_{tip} at constant $r_{\text{dot}} = 25\,\text{nm}$. **(c)** Sketch of the total capacitance of the dot C_Σ, composed of $C_\Sigma = C_{\text{tip}} + C_{\text{BG}} + C_{\text{gr}} = 8\,\text{aF} + 5\,\text{aF} + 3.5\,\text{aF} = 16.5\,\text{aF}$, and the tunneling resistances of dot states to the tip R_{tip} and to the surrounding graphene R_{gr}, where $R_{\text{tip}} \gg R_{\text{gr}}$.

After computing the confined states in the TB model, we are interested in their capacitive couplings. We model the capacitances with the help of the Poisson solver using a disk of radius $r_{\text{dot}} = 25 \pm 5\,\text{nm}$, deduced from Figure S3c, with the DOS of graphene and an additional counter electrode being either the tip, the surrounding graphene separated by an insulating ring of width w_{gap} or the graphite back-gate (see Fig. S3c). In case of the dot-tip capacitance C_{tip} and the dot-back-gate capacitance C_{BG}, the tip and back-gate were set to a fixed potential, respectively, and the induced charge on the QD was used to deduce the capacitances. For the capacitance of the dot to the surrounding graphene C_{gr}, the dot potential was fixed and the induced charge within a cut-off radius of $50\,\text{nm}$ into the bulk was used.

For the combination of $r_{\text{dot}} = 25 \pm 5\,\text{nm}$, $r_{\text{tip}} = 120^{+30}_{-20}\,\text{nm}$ and $w_{\text{gap}} = 10 \pm 5\,\text{nm}$, we

find at $V_{\text{tip,eff}} = -0.2\,\text{V}$ values of $C_{\text{tip}} = 8 \pm 1.5\,\text{aF}$, $C_{\text{BG}} = 5 \pm 1\,\text{aF}$, $C_{\text{gr}} = 3.5 \pm 0.7\,\text{aF}$ and thus $C_{\Sigma} = 16.5 \pm 3.2\,\text{aF}$. The errors result from varying r_{dot} and r_{tip}, which dominate over the impact of w_{gap}. Their influence on $\alpha_{\text{tip}} = C_{\text{tip}}/C_{\Sigma}$, which is the important quantity for conversion from tip voltage distances to addition energies, is portrayed in Figure S4. Although graphene's DOS ensues energy dependent capacitances (so-called quantum capacitance), they obviously all show a similar behaviour and thus α_{tip} remains nearly constant away from the Dirac point. Especially in the relevant regime of the observed charging peaks, i.e., $V_{\text{tip,eff}} < -150\,\text{mV}$, we find $\alpha_{\text{tip}} = 0.51 \pm 0.03$.

We also note that the confined states tunnel-couple more strongly laterally to the bulk graphene states than to the tip, since the tunneling resistance to the tip R_{tip} is of the order of GΩ and thereby exceeds that to the graphene bulk R_{gr} (several h/e^2) by orders of magnitude. Thus we also neglect any additional resistances in series (Au-electrode, graphite, bulk graphene) or any effect of the local density of states of bulk graphene or graphite. Vertical tunnel-coupling of the QD states to the graphite electrode is virtually null due to the 30 nm thick BN flake.[9]
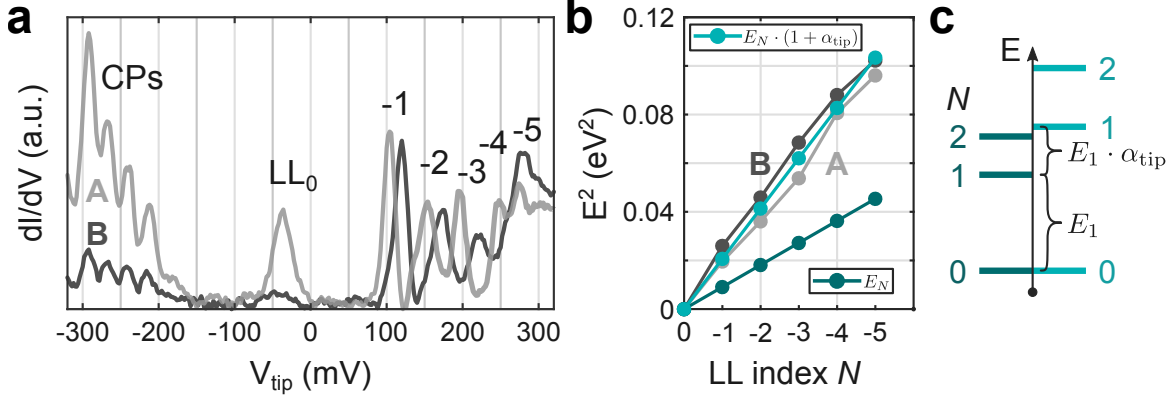
5 Landau levels and estimation of the Fermi energy

Figure S5: **(a)** dI/dV spectra, averaged over trace and retrace, recorded at $B = 7\,\mathrm{T}$, $V_\mathrm{stab} = 400\,\mathrm{mV}$ and $I_\mathrm{stab} = 200\,\mathrm{pA}$. Contributions from states with $m = 0$ originating from LLs with $N = 0, \ldots, -5$ are marked, as well as charging peaks (CPs). Contribution from LL_{-4} for spectrum B only visible as shoulder. **(b)** Comparison of the squared measured peak energies deduced from **a** (light and dark gray) to the squared ideal LL energies (E_N, petrol) calculated from eq 1 ($\nu_\mathrm{F} = 1 \times 10^6\,\mathrm{m/s}$) of the main text. Additionally the calculated values are plotted after multiplication with a factor of $1 + \alpha_\mathrm{tip} = 1.51$ (cyan). **(c)** Schematic of the ideal LL energies (left) and expected energies in dI/dV (right), where the latter are shifted by the gating effect of the tip to $(1 + \alpha_\mathrm{tip})$-times larger energies.

For some tips we find dI/dV spectra portraying an apparent LL sequence at $B = 7\,\mathrm{T}$ like in Figure S5a for $V_\mathrm{tip} > -100\,\mathrm{mV}$. We do not observe LLs for $V_\mathrm{tip} < -100\,\mathrm{mV}$ since charging peaks set on earlier for $V_\mathrm{tip} < 0$, which in turn is due to LL_{-1} being closer to E_F than LL_{+1} (see discussion of asymmetric onset of charging peaks in the main text). Plotting the squared LL peak energies for spectra A and B in Figure S5b, we see that they do not correspond to the ideal LL energies (E_N) of eq 1 of the main text, using $\nu_\mathrm{F} = 1 \times 10^6\,\mathrm{m/s}$. However, they show a square root dependency and if we include the gating effect of the tip by multiplying E_N by $1 + \alpha_\mathrm{tip} = 1.51$ (schematically Fig. S5c), we see agreement. We conclude that the dI/dV features have to originate from states which are gated by the tip, thus they need to be sufficiently localized underneath the tip and we do not probe the bulk LLs. The distinct peaks in the spectra may be explained by dominant contributions to dI/dV from the states with $m = 0$ (peak in the wave function amplitude at $r = 0$) originating from the respective LLs.[10,11] These are not the confined QD states responsible for the charging peaks in the

positive sector (electron confinement), as these already occupied states will not cross E_F. Dominating $m = 0$ states are only observed if (i) the tip tunnels very close to its capacitive center and (ii) the confining potential is very close to circularly symmetric around this center. If either condition is flawed, various angular momentum states will contribute to dI/dV and multiple peaks per LL will be observed.[11] Quantitatively, misalignment smaller than the magnetic length will already lead to significant contributions of $m \neq 0$ states (compare line cuts in Fig. S7b-d). As charging patterns in maps of the dI/dV signal reveal the same symmetry as the graphene superstructure, we can estimate the relative shift of tunneling and capacitive center. We commonly find shifts of about $5\,\mathrm{nm}$. This explains why the majority of dI/dV spectra feature a very rich structure in the charging peak 'gap'. However, without knowing the exact confinement potential everywhere, linking spatially varying contributions of the peaks to distinct m states cannot be done reliably. Since we find LL_0 peaks always in the unoccupied states sector (i.e., $V_\mathrm{tip} < 0\,\mathrm{V}$), we use $E_\mathrm{F} = -40 \pm 5\,\mathrm{meV}$ (Fig. S5a) to determine the coincidence of states with E_F in the TB calculations.

Finally, we note that the states visible as charging peaks cannot be probed at the chemical potential of the tip directly, because a positively charged tip ($\mu_\mathrm{tip} < \mu_\mathrm{graphene}$) will lead to confinement of states from above the graphene Fermi level for increasing band bending and vice versa.
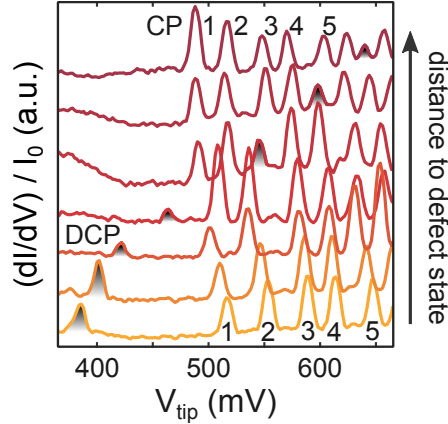
6 Identification of defect charging peaks

Figure S6: dI/dV spectra, normalized by initial current I_0, recorded while laterally moving the tip away from a defect state. Top spectrum is 16.5 nm further away than the bottom one. $V_{stab} = 1\,V$, $I_{stab} = 700\,pA$, $V_{mod} = 4.2\,mV_{rms}$ and $B = 7\,T$. The charging peak originating from the defect state is highlighted and labeled DCP, and the first five charging peaks of the tip-induced QD are marked CP1-5.

In Figure 2c of the main text we see the median values of the charging peak distances for electrons deviate from the clear quadruplet sequence for confined holes in Figure 2b of the main text. This is due to defect charging peaks (DCPs), which most probably stem from charging of localized states in the BN, showing up as ring like structures in dI/dV maps. These 'ring defects' were previously observed by Wong et al.[12] and attributed to carbon impurities in the topmost BN layer. The respective defect level lies above the Dirac point, which agrees with our almost exclusive observation of DCPs for positive V_{tip}.

In contrast to charging of tip-induced QD states, V_{tip} needs to be increased to charge the same defect state as the tip moves away, since the capacitive coupling to the state weakens. Such a sequence of dI/dV spectra, where the tip laterally shift its position away is portrayed in Figure S6. As soon as the DCP mixes with the QD charging peaks, the charging peak sequence will be offset by one. From which index on a specific spectrum is offset depends on the distance to the defect state, where the spectrum is recorded. This blurs the fourfold sequence of the median values in Figure 2c of the main text, since for higher charging peak indexes, that is, higher V_{tip}, spectra in a larger area around the defect will incorporate

the corresponding DCP. The ideal quadruplet transitions for the median values washes out and later even shift towards higher peak transition indexes (Fig. 2c of the main text, e.g., $12 \rightarrow 13$, $16 \rightarrow 17$).
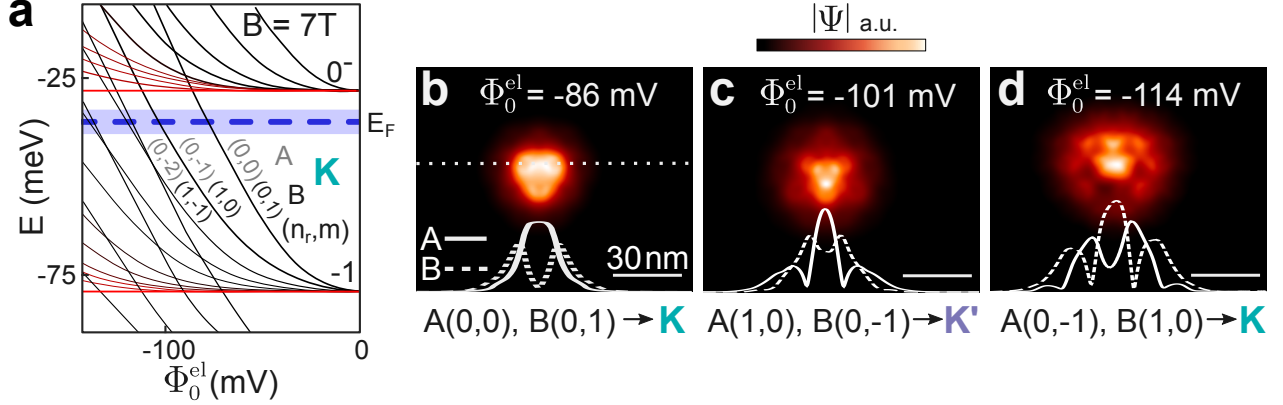
7 Assigning a valley to the TB wave functions

Figure S7: **(a)** Schematic of state energies for valley K deduced from Fig. 4a of the main text. LL_{0^-} and LL_{-1} are marked. Blue horizontal bar marks uncertainty in E_F. State labels correspond to radial and angular momentum quantum number (n_r, m) on sublattice A and B colored differently as marked. **(b-d)** Color plot of $|\Psi|$ of the first, third and fourth state crossing E_F on the hole side. Φ_0^{el} at the crossing point $\varepsilon_i(\Phi_0^{el}) = E_F$ is marked. Solid (dashed) white lines are line cuts along the dotted white line in **b** for contributions from sublattice A (B), as marked. Below the plots, (n_r, m) combinations on sublattice A and B, and associated valley (eq 2 main text) are added. All scale bars identical.

In order to classify our TB wave functions in terms of N, n_r and m, we consider sublattice A and B separately. Tracing the states back to their LL of origin reveals N, constraining possible $n_r \leq N$. The value of n_r is then determined by counting radial minima in sublattice dependent line cuts of the wave function amplitude (Fig. S7b-d and Fig. 4b-d of the main text). The distance of the first radial maximum from the center of the wave function is finally sufficient to order the possible m numbers of the LL (eq 3 of the main text). Additionally, the (n_r, m) combinations need to be consistent with N differing by one on the two sublattices (eq 2 of the main text). As shown in the main text for the first pair of states, the roles of the two sublattices also interchanges for the second pair of states (compare Fig. S7c,d). Inserting n_r and m in eq 2 of the main text yields the valley index, where states with $N_A = N_B - 1$ and $N_B = N_A - 1$ are assigned to valley K and K', respectively. We note that the valley index orders as K-K' for the first pair of states and as K'-K for the second on the AA-stacked area. For valley K more states are labeled by their (n_r, m) combinations in Figure S7a.

References

(1) Mayorov, A. S.; Gorbachev, R. V.; Morozov, S. V.; Britnell, L.; Jalil, R.; Pono-
   marenko, L. A.; Blake, P.; Novoselov, K. S.; Watanabe, K.; Taniguchi, T.; Geim, A. K.
   Nano Lett. **2011**, *11*, 2396–2399.

(2) Kretinin, A. V. et al. *Nano Lett.* **2014**, *14*, 3270–3276.

(3) Woods, C. R. et al. *Nat. Phys.* **2014**, *10*, 451–456.

(4) Voigtländer, B.; Cherepanov, V.; Elsaesser, C.; Linke, U. *Rev. Sci. Instrum.* **2008**, *79*,
   033911.

(5) Dombrowski, R.; Steinebach, C.; Wittneven, C.; Morgenstern, M.; Wiesendanger, R.
   Phys. Rev. B **1999**, *59*, 8043–8048.

(6) Chen, Y. C.; Zhao, C. C.; Huang, F.; Zhan, R. Z.; Deng, S. Z.; Xu, N. S.; Chen, J. *Sci.
   Rep.* **2016**, *6*, 21270.

(7) Maksym, P. A.; Roy, M.; Craciun, M. F.; Russo, S.; Yamamoto, M.; Tarucha, S.;
   Aoki, H. *J. Phys. Conf. Ser.* **2010**, *245*, 012030.

(8) Giavaras, G.; Nori, F. *Phys. Rev. B* **2012**, *85*, 165446.

(9) Britnell, L.; Gorbachev, R. V.; Jalil, R.; Belle, B. D.; Schedin, F.; Katsnelson, M. I.;
   Eaves, L.; Morozov, S. V.; Mayorov, A. S.; Peres, N. M. R.; Neto, A. H. C.; Leist, J.;
   Geim, A. K.; Ponomarenko, L. A.; Novoselov, K. S. *Nano Lett.* **2012**, *12*, 1707–1710.

(10) Morgenstern, M.; Haude, D.; Gudmundsson, V.; Wittneven, C.; Dombrowski, R.;
    Wiesendanger, R. *Phys. Rev. B* **2000**, *62*, 7257–7263.

(11) Luican-Mayer, A.; Kharitonov, M.; Li, G.; Lu, C. P.; Skachko, I.; Goncalves, A. M.;
    Watanabe, K.; Taniguchi, T.; Andrei, E. Y. *Phys. Rev. Lett.* **2014**, *112*, 036804.

(12) Wong, D.; Velasco, J., Jr.; Ju, L.; Lee, J.; Kahn, S.; Tsai, H. Z.; Germany, C.; Taniguchi, T.; Watanabe, K.; Zettl, A.; Wang, F.; Crommie, M. F. *Nat. Nanotechnol.* **2015**, *10*, 949–953.